

Novel Magnetic Nanostructures for Advanced Hyperthermia

by

Deborah Israel
deborah19@mail.usf.edu
U59886347

Director: Manh-Huong Phan, PhD
Committee: Raja Das, PhD

Department of Physics
University of South Florida
Submitted April 15th, 2016

Acknowledgments

I would first like to thank my thesis director, Dr. Manh-Huong Phan, for his instruction and encouragement every step of the way. I'd also like to thank Raja Das for introducing me to iron cobalt nanocubes and instructing me through countless synthesis procedures and Kristen Repa for helping me join the Functional Materials Lab, teaching me everything I know about carbon nanotubes and magnetic nanoparticles, and being a fantastic mentor. In addition, I have to thank Dr. Hariharan Srikanth for inviting me to join FML two years ago. I'd also like to acknowledge all of the other members of the FML group for their encouragement, assistance throughout this entire process. I want to give a special thanks to Dr. Robert Hyde of the physics department for training me on many pieces of department equipment and Dr. Edward Haller of the integrated biology department for training me and helping me operate the Transmission Electron Microscope. In addition, I want to thank our collaborators from Prof. Manuel Vazquez's group at Instituto de Ciencia de Materiales de Madrid, who helped in our synthesis of CNTs. Finally, I want to give a big thank you to everyone in the USF Physics Department.

Contents

1	Introduction	1
1.1	Problem and Motivation	1
1.2	Overview of Magnetism	3
1.3	Magnetic Hyperthermia	4
2	Synthesis Procedures	7
2.1	Magnetic Nanoparticles	8
2.2	Carbon Nanotubes	11
2.3	Iron-Cobalt Nanocubes	14
3	Characterization Techniques	16
3.1	Structure and Morphology	16
3.1.1	X-Ray Diffraction	16
3.1.2	Microscopy	17
3.2	Magnetic Measurements	19
3.3	Hyperthermia	21
4	Results	22
4.1	Structure, Morphology and Magnetic Properties	22
4.1.1	Nickel Ferrite Nanoparticles	22
4.1.2	Nanoparticle-Filled Carbon Nanotubes	24
4.1.3	Iron-Cobalt Nanocubes	26
4.2	Hyperthermia	29
5	Conclusion	32
5.1	Conclusion of Current Work	32
5.2	Future Work	33
A	References	35

List of Figures

1.1	Example of the hysteresis loop of a ferromagnetic material (taken from ref. [37]).	3
1.2	Graphic showing the magnetic hyperthermia technique (taken from ref. [38]).	4
2.1	A simple graphic demonstrating the co-precipitation synthesis technique (taken from ref. [39]).	8
2.2	A simple graphic demonstrating the microemulsion synthesis technique (taken from ref. [40]).	9
2.3	A simple graphic demonstrating the hydrothermal synthesis technique (taken from ref. [39])	10
2.4	A simple graphic demonstrating the thermal decomposition synthesis technique (taken from ref. [41])	10
2.5	Graphic demonstrating the arc-discharge method of CNT synthesis (taken from ref. [27]).	11
2.6	Graphic demonstrating the laser ablation method of CNT synthesis (taken from ref. [27]).	12
2.7	Graphic showing the set-up for the gas-phase catalytic growth synthesis method (taken from ref. [30]).	13
2.8	Graphic showing the procedure for making nanoparticle-filled carbon nanotubes: (i) alumina template (ii) CNTs grown inside the template (iii) CNTs filled with ferrofluid via magnetically-assisted capillary action (iv) CNTs filled with nanoparticles. (taken from ref. [20])	15
3.1	Graphic demonstrating Bragg diffraction in XRD (taken from ref. [33]).	17
3.2	Schematic of a transmission electron microscope (taken from ref. [35]).	18
3.3	Schematic of a vibrating sample magnetometer (taken from ref. [42])	20
4.1	X-Ray Diffraction plot for NiFe_2O_4 nanoparticles.	23
4.2	Transmission Electron Microscope image of nickel ferrite nanoparticles.	23
4.3	TEM image of CNTs.	24
4.4	TEM image of nanoparticle-filled CNTs.	24
4.5	Normalized hysteresis curves for the NiFe_2O_4 nanoparticles and filled CNTs with inset comparing the saturation magnetization of the two samples.	25
4.6	Plot showing the diffraction patterns for the FeCo sample.	26
4.7	TEM images of FeCo nanocubes from the (a) 30 minute, (b) 40 minute, and (c) 50 minute reaction.	27

4.8	Hysteresis curves for the (a) 141 nm, (b) 262 nm, and (c) 340 nm cubes. . .	28
4.9	Heating curves for the (a) 141 nm, (b) 262 nm, and (c) 340 nm cubes. . . .	29
4.10	Graph studying the size-dependence of the SAR in FeCo nanocubes.	30

Abstract

Growing interest in magnetic nanoparticles for magnetic hyperthermia has researchers investigating nanostructures for their potential application to magnetic hyperthermia. Carbon nanostraws filled with magnetic nanoparticles and iron cobalt nanocubes are novel materials whose magnetic properties (high saturation magnetization, high anisotropy and high aspect ratio) make them a promising candidate for magnetic hyperthermia. In this thesis, we have compared the potential of nickel ferrite nanoparticles and nickel ferrite filled carbon nanotubes for magnetic hyperthermia applications. We have also performed a study on the influence of size on the heating properties of iron cobalt nanocubes. Overall, our study demonstrates that nanoparticle-filled carbon nanotubes and iron cobalt nanocubes are promising candidates for magnetic hyperthermia.

Chapter 1

Introduction

1.1 Problem and Motivation

Cancer caused over half a million deaths in the United States last year.¹ In addition, about 40 percent of people will be diagnosed with some kind of cancer in their lifetime.² The occurrence of death and diagnoses of cancer have been in a slow but steady decline for the last thirty years, but in some types of cancers, rates of death have become stagnant or have even increased. Furthermore, in President Obama's 2016 State of the Union address, he urged American scientists to find the cure for cancer.³

Finding the cure for cancer will not be an easy task. Currently, there are three major treatment options for cancer: surgery, chemotherapy, and radiation therapy.⁴ Each treatment type has its own advantages and pitfalls.

Surgery has shown to be extremely effective when it comes to treating a localized tumor. On the other hand, surgery is not very effective in treating cancer that has metastasized. Additionally, depending on the size and anatomy of a specific tumor, surgery could be

impractical.⁵ Surgery is also very invasive and, even with minor surgical procedures, the patient risks pneumonia, bleeding, infection, and death.⁶

Chemotherapy is a blanket term used to describe the use of drugs to combat cancer. These drugs are effective at slowing the growth and sometimes killing cancer cells, especially in cancers that have metastasized.⁷ Still, there are drawbacks. Certain medications a patient may be taking prior to treatment may have problematic interactions with chemotherapy drugs. Chemotherapy can also cause undesirable side effects such as nausea, vomiting and hair loss.⁸

Radiation therapy is another treatment that is effective at shrinking localized tumors. Unlike chemotherapy, it isn't very effective at treating cancer that has spread and it can be much more costly.⁹ Radiation side effects include fatigue, skin changes, and loss of appetite.¹⁰

Due to the flawed nature of these treatments, there is a big push to find new, innovative ways to treat cancer, such as clinical hyperthermia. Clinical hyperthermia is the use of heat to kill cancer cells. It is often used synergistically with chemotherapy, radiation, and surgery in order to shrink tumors or slow cancer growth.¹¹ Current methods of clinical hyperthermia have run into some issues. In the use of deep tissue tumors, it can be very awkward to deliver a therapeutic dose of heat. Additionally, systemic treatment isn't effective enough to replace chemotherapy and radiation therapy. Finally, there are issues with treating only the cancer cells while leaving surrounding, healthy tissue unharmed. For that reason, magnetic hyperthermia is being researched as a promising method of clinical hyperthermia.¹²

1.2 Overview of Magnetism

There are many different types of magnetism. The difference between the separate types lies in how the magnetization (M) of a material responds to an external magnetic field (H), as well as how individual magnetic dipoles are arranged in the material.¹³ In paramagnetic and diamagnetic materials, magnetic moments will either line up with (paramagnetic) or oppose (diamagnetic) any external field applied to them, but they will not retain any permanent magnetization due to the lack of interaction in the magnetic dipoles of the material.¹⁴ These materials are often referred to as nonmagnetic.

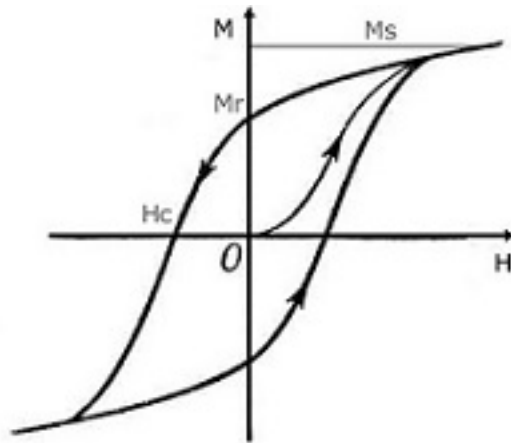


Figure 1.1: Example of the hysteresis loop of a ferromagnetic material (taken from ref. [37]).

Ferromagnetic, ferrimagnetic, and antiferromagnetic materials, however, have interactions between their magnetic dipoles and will retain magnetization. Due to this, materials exhibit a behavior called hysteresis and a plot of magnetization as a function of external field is called a hysteresis loop (Figure 1.1).¹⁵ A hysteresis loop demonstrates unique magnetic properties. Saturation magnetization (M_S) occurs when the magnetic moments of a material all line up with the external magnetic field. When the external magnetic field is then reduced to zero,

the remaining magnetization is referred to as M_R . Coercivity (H_C) is the external magnetic field required to reduce the magnetization to zero after saturation magnetization.^{13,14}

Superparamagnetism is achieved when the size of a ferro- or ferrimagnetic material is reduced to a critical size. When this happens, these materials begin exhibiting paramagnetic properties, including zero coercivity and remnant magnetization. However, unlike paramagnetic materials, superparamagnetic materials exhibit a higher saturation magnetization.¹⁶

1.3 Magnetic Hyperthermia

Magnetic hyperthermia is an attractive option for cancer treatment. In this method, a patient would be injected with magnetic nanostructures and an external alternating current (AC) magnetic field is applied (see Fig. 1.2). When the nanostructures are exposed to this AC field, eddy currents, hysteresis losses, and relaxation losses are able to generate a therapeutic dose of heat.¹²

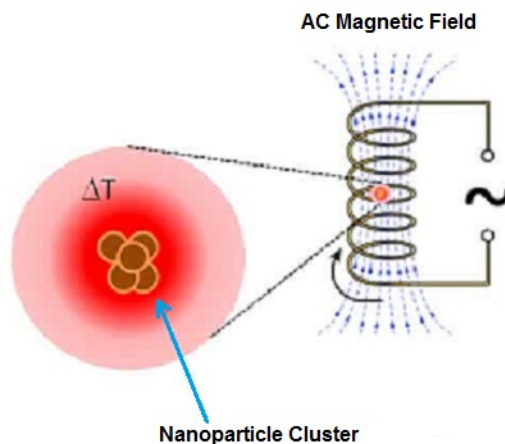


Figure 1.2: Graphic showing the magnetic hyperthermia technique (taken from ref. [38]).

Magnetic hyperthermia can alleviate some of the problems that have been encountered

with other methods of clinical hyperthermia. Advances in chemistry have made it so that magnetic nanoparticles can be specifically targeted at cancer cells, making magnetic hyperthermia a truly local treatment. In addition, due to the small area of the treatment, the nanoparticles can be heated to a temperature high enough to kill the cancer cells while keeping surrounding tissue unaffected.¹²

In order to compare different materials, it is necessary to define a parameter that describes how these materials respond to external AC fields. As such, most hyperthermia experiments use a parameter called the specific absorption rate (SAR). The SAR can be described as the absorption of electromagnetic energy per unit mass when exposed to a particular field frequency. The SAR can be mathematically defined as follows:

$$SAR = \frac{C\rho}{\phi} \frac{\Delta T}{\Delta t}, \quad (1.1)$$

where C is the specific heat of the solvent, ρ is the density of the solvent, ϕ is the concentration of the sample, and $\frac{\Delta T}{\Delta t}$ is the change of temperature over the change in time.¹⁷

Since the majority of absorbed energy comes from hysteresis, we can estimate the SAR in terms of the properties of the applied AC field and material by directly calculating the hysteresis losses, which is proportional to the area of the hysteresis loop.¹⁸ In the ideal case, the SAR could be estimated as follows:

$$SAR = 4\alpha\mu_0 H_{app} f_{exc} M_S, \quad (1.2)$$

where α is a constant describing the squareness of the hysteresis loop, μ_0 is the permeability of free space, H_{app} is the magnitude of the external magnetic field, f_{exc} is the frequency

of the external magnetic field and M_S is the saturation magnetization.¹⁹ As such, it would be optimal to analyze materials that have a very square hysteresis loop, high saturation magnetization, and high coercivity.^{19,20} For this reason, this thesis will investigate the potential of nickel ferrite nanoparticles, nanoparticle filled carbon nanotubes, and iron cobalt nanocubes for magnetic hyperthermia applications.

Chapter 2

Synthesis Procedures

In this chapter, we discuss the synthesis procedures for the materials used in this thesis. We begin with an overview for the synthesis of NiFe_2O_4 magnetic nanoparticles. We then present multiple techniques for carbon nanotube (CNT) synthesis, then go into the method used to fill the CNTs with magnetic nanoparticles. Then, we will go over the synthesis and size-variation of FeCo nanocubes.

These materials were selected for a variety of reasons. Magnetic nanoparticles were chosen for their easy synthesis and functionalization in addition to their superparamagnetic properties.¹⁸ Carbon nanotubes filled with nanoparticles were selected due to their high aspect-ratio and enhanced superparamagnetic properties²⁰. FeCo nanocubes were chosen for their ferromagnetic properties, high saturation magnetization, and high anisotropy.²¹

2.1 Magnetic Nanoparticles

There are a variety of ways to synthesize magnetic nanoparticles, which can change the size, shape, and magnetic properties of the nanoparticles. In addition, different procedures change how the surfaces of nanoparticles are coated, therefore changing the solvent that they are able to be suspended in. The commonly used techniques include co-precipitation, microemulsion, hydrothermal, and thermal decomposition.²²

Co-precipitation is a fast and convenient method for iron oxide synthesis where a basic solution is added to an iron salt (Fe^{2+} or Fe^{3+}) solution at a relatively low temperature (see Fig. 2.1). This results in an instant reaction and the products will split into a precipitate and a supernatant. The precipitate is then washed via centrifugation in the presence of ethanol or water. After this step, only iron oxide nanoparticles will remain.²³ While this method is useful in its relative ease, it is very difficult to control the particle size, resulting in a large size distribution.^{22,23}

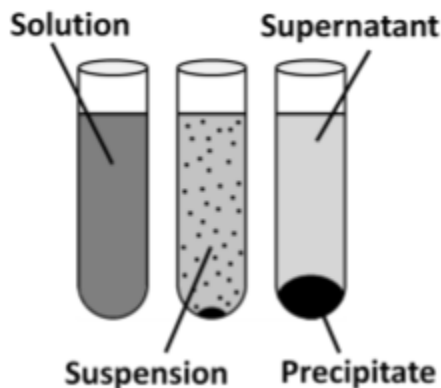


Figure 2.1: A simple graphic demonstrating the co-precipitation synthesis technique (taken from ref. [39]).

Microemulsion, on the other hand, allows for easy and precise control over the shape and size of nanoparticles. In this technique, two immiscible liquids are added together in the

presence of iron salts to form microdroplets. This process is done twice separately, forming the reactants. These are then mixed together and the microdroplets interact to form a precipitate (see Fig. 2.2). The product is then left to reflux and centrifuged to isolate the nanoparticles.²⁴ Even though this method allows for a large amount of control, it produces a very small amount of nanoparticles.²²

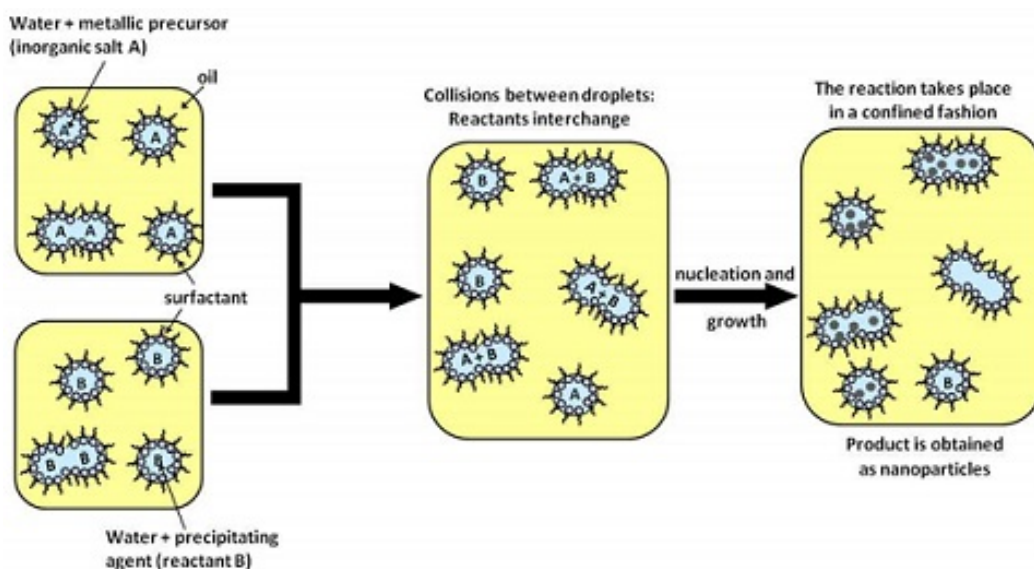


Figure 2.2: A simple graphic demonstrating the microemulsion synthesis technique (taken from ref. [40]).

Hydrothermal synthesis works by taking reactants and putting them in a high pressure environment at a high temperature for a period of up to 72 hours.²⁵ This method allows large particles to be produced with a very narrow size distribution (see Fig. 2.3). However, much like microemulsion, it produces a small amount of nanoparticles.²²

Thermal decomposition works by breaking down reactants at high temperatures to form new materials. To synthesize nanoparticles by thermal decomposition, an organometallic compound (typically a metal acetylacetonate) is mixed with a surfactant and organic solvent, then heated to a high temperature (see Fig. 2.4).²⁶ This procedure is quick and allows for

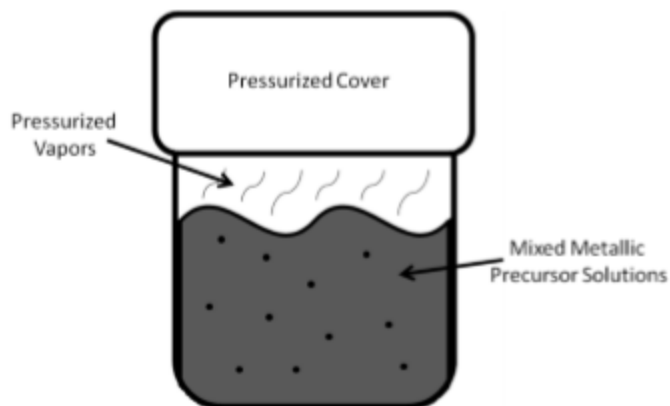


Figure 2.3: A simple graphic demonstrating the hydrothermal synthesis technique (taken from ref. [39])

easy control of size and shape.²²

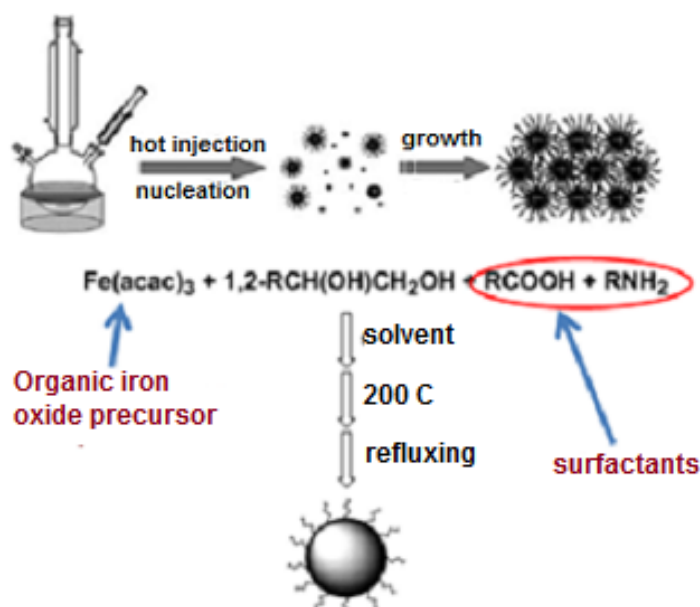


Figure 2.4: A simple graphic demonstrating the thermal decomposition synthesis technique (taken from ref. [41])

For this thesis, thermal decomposition was used to synthesize nanoparticles due to the high yield of nanoparticles and tunability of their size and shape. Nickel ferrite was synthesized by combining 1 mmol of nickel acetylacetonate ($\text{Ni}(\text{acac})_2$), 2 mmol of iron acetylacetonate ($\text{Fe}(\text{acac})_3$), 10 mmol of 1,2-hexadecanediol, 6 mmol of oleic acid, 6 mmol of

oleyl amine and 20 mL of benzyl ether in a three-necked flask. Under a blanket of argon, the reactants were magnetically stirred and heated to 200°C for 2 hours, then heated to reflux at 300°C for an hour. The precipitate was separated by centrifugation and suspended in hexane.

2.2 Carbon Nanotubes

Synthesis methods of carbon nanotubes include arc-discharge, laser ablation, gas-phase catalytic growth, and chemical vapor deposition.²⁷

In the arc-discharge method, two graphite rods are brought together to serve as an anode and cathode (see Fig. 2.5). Under a helium atmosphere, a voltage is applied and increased until a stable arc of current is formed. Material builds up on the cathode, forming carbon nanotubes and carbon particles.²⁸

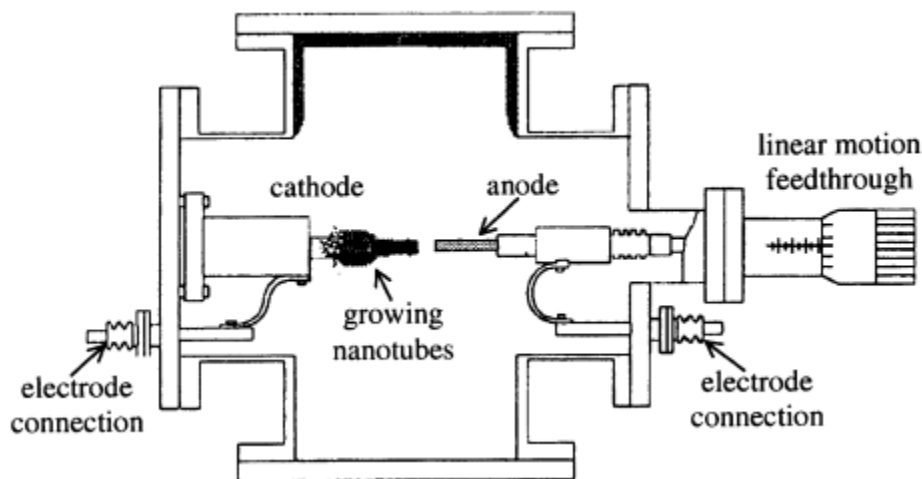


Figure 2.5: Graphic demonstrating the arc-discharge method of CNT synthesis (taken from ref. [27]).

In the laser ablation method, a graphite source is placed into a flow tube with a high temperature argon environment (see Fig. 2.6). A laser is then pointed in the same direction

as the flow of argon and aimed at the graphite source, vaporizing the graphite. The argon then carries the vaporized carbon to the other end of the tube, where it condenses and deposits on the walls of the tube.²⁹

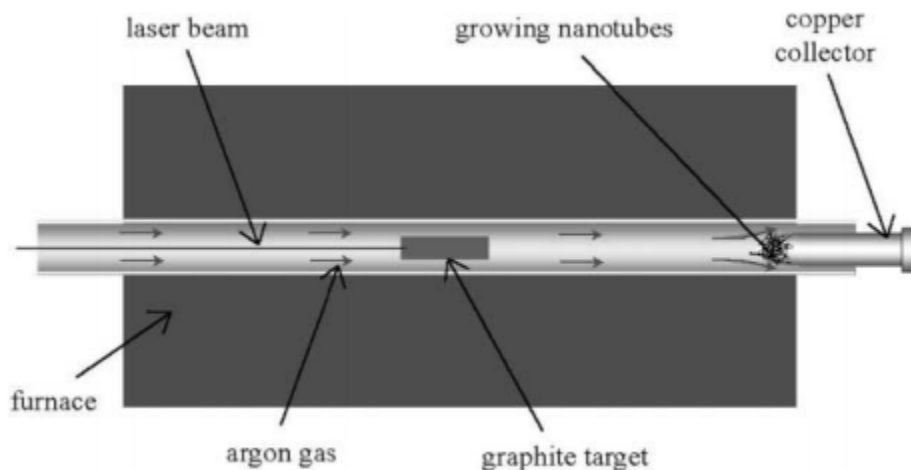


Figure 2.6: Graphic demonstrating the laser ablation method of CNT synthesis (taken from ref. [27]).

Both the arc-discharge and laser ablation present considerable disadvantages. These techniques produce a small volume of sample and additional purification steps are required after synthesis to get rid of unwanted impurities.²⁷

Other methods for synthesized carbon nanotubes are referred to as gas-phase techniques. These techniques fix many of the issues with arc-discharge and laser ablation methods. The gas-phase technique uses a carbon source that is continually replaced by flowing gas, allowing for a higher yield of nanotubes. In addition, the final products have a higher purity and do not requiring fewer purification steps.²⁷

One gas-phase technique, called gas-phase catalytic growth, uses carbon monoxide as the carbon source (see Fig. 2.7). In this technique, carbon monoxide mixed with a small amount of $\text{Fe}(\text{CO})_5$ flows through a high temperature, high pressure reactor, forming iron clusters

on which the CNTs nucleate and grow. In order for the highest yield of CNTs, this reaction occurs at a temperature of 1200° C and pressure of 10 atm. This results in a high yield of extremely pure CNTs.³⁰

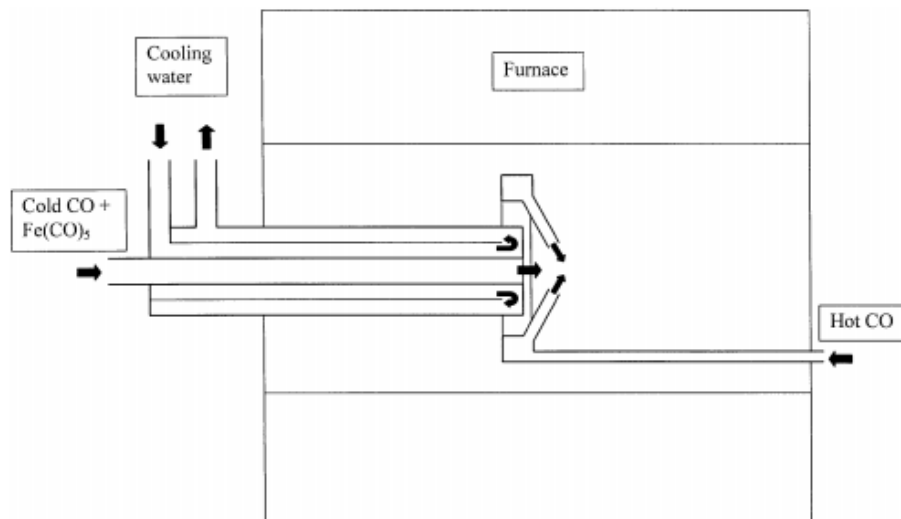


Figure 2.7: Graphic showing the set-up for the gas-phase catalytic growth synthesis method (taken from ref. [30]).

Chemical vapor deposition (CVD) uses hydrocarbon gases as a carbon source. There are many ways of synthesizing CNTs using CVD, including plasma-enhanced chemical vapor deposition, microwave plasma-enhanced CVD, and thermal CVD. In each method, hydrocarbon gases flow through a tube furnace that has been heated to about 600-700°C, where CNTs are able to grow. CVD allows for a high level of morphological control and produces a large quantity of CNTs.^{20,27}

Due to the high level of control, a thermal CVD technique was used to synthesize carbon nanotubes for this thesis. In this method, CNTs are grown inside the pores of alumina template membranes. The alumina template membranes for this thesis were fabricated via anodization. Prior to the synthesis of the CNTs, the alumina templates are placed between two quartz slides and heated to 740°C for 1 hour to prevent the templates from bending

during synthesis. The template is then placed vertically in a tube furnace and heated to 670°C under the flow of argon. When the temperature reaches 670°C, the argon gas is turned off and replaced with a flow of helium (flow rate 70 sccm) and ethylene (flow rate 30 sccm). The reaction is left to run for 6 hours, then gas flow is switched back to argon and the furnace is allowed to cool to room temperature. When the furnace reaches room temperature, the argon gas is turned off.

After the CNTs are synthesized, they are filled with nanoparticles. Before filling the nanotubes, a permanent magnet is placed under the CNT-filled alumina templates. Nanoparticles suspended in hexane are then poured drop-wise on the top end of the CNT-filled alumina templates. The CNTs are then filled with nanoparticles via magnetically assisted capillary action. After the hexane evaporated, the template is broken and dissolved in a 4.0 M NaOH solution, then sonicated. The solution is then filtered through a polyester nucleopore membrane and washed with isopropanol and deionized water. Finally, the CNTs are allowed to dry at room temperature. Figure 2.8 shows a procedure for making nanoparticle-filled carbon nanotubes.

2.3 Iron-Cobalt Nanocubes

The Iron-Cobalt nanocubes for this thesis were synthesized using a liquid-phase reduction reaction described by Kolhatkar, et al.^{21,31}

In this method, 0.72 g of $\text{FeSO}_4 \cdot 7\text{H}_2\text{O}$, 0.64 g of $\text{CoCl}_2 \cdot 6\text{H}_2\text{O}$, 6.1 mL of poly(ethylene glycol) ($\text{mw} \approx 400$ g), 0.8 mL of cyclohexane, and 50 mL of water are combined in a flask and sonicated for 90 minutes in an argon atmosphere. This solution is then heated to 78°C

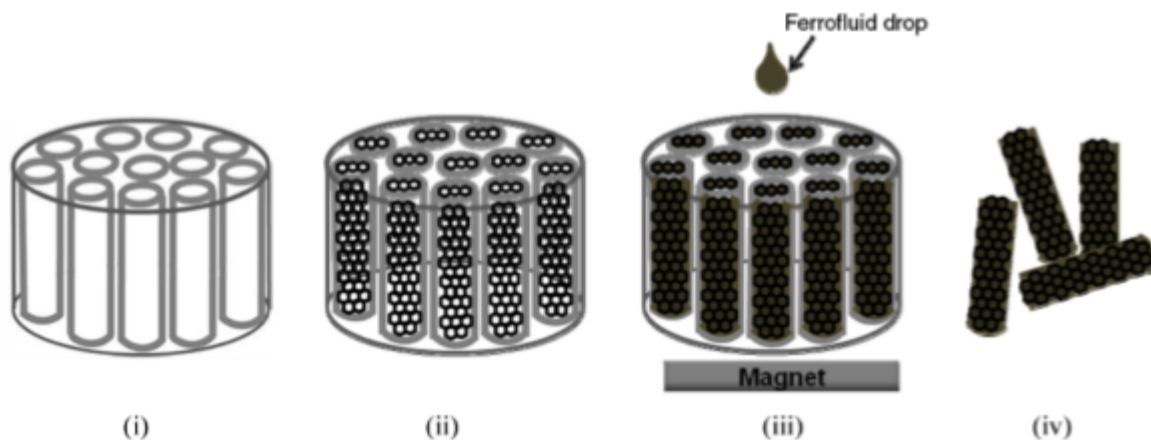


Figure 2.8: Graphic showing the procedure for making nanoparticle-filled carbon nanotubes: (i) alumina template (ii) CNTs grown inside the template (iii) CNTs filled with ferrofluid via magnetically-assisted capillary action (iv) CNTs filled with nanoparticles. (taken from ref. [20])

and a second solution composed of 20 mL of hydrazine and 2.5 g of NaOH is added. After a reaction of 30-50 minutes, the products were washed by centrifugation in the presence of water three times, then washed in the presence of acetone and toluene. Finally, the resulting FeCo nanocubes are dried at room temperature.

Chapter 3

Characterization Techniques

In this chapter, we will be going over the various techniques used to characterize the samples described in Chapter 2. These include structural and morphological measurements, such as x-ray diffraction and microscopy, magnetic measurements, and hyperthermia measurements.

3.1 Structure and Morphology

3.1.1 X-Ray Diffraction

X-ray diffraction (XRD), as the name implies, utilizes the diffraction of x-rays off of a crystalline lattice. In this method, incident x-rays on the sample bounce off of atoms in a lattice and are gathered by a detector (see Fig. 3.1).³² Interference coming from differences in path length can be described by the Bragg equation:

$$n\lambda = 2d \sin \theta, \tag{3.1}$$

where n is a non-zero positive integer, λ is the wavelength of the incident x-rays, d is the lattice spacing, and θ is the angle of incidence.³³ The diffracted x-rays interact with each other and make diffraction patterns, which show up as a series of peaks in different locations depending on the lattice spacing of the sample.^{32,33}

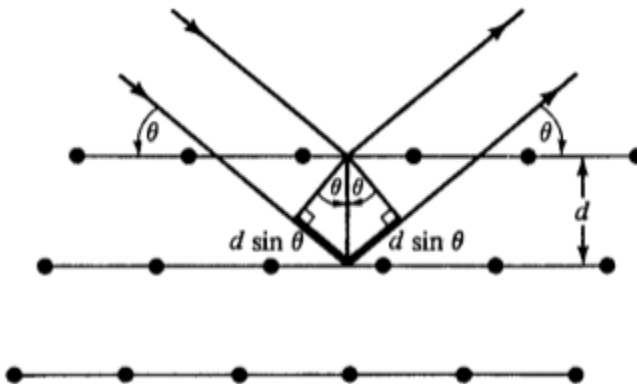


Figure 3.1: Graphic demonstrating Bragg diffraction in XRD (taken from ref. [33]).

To prepare samples for XRD, we created a thin film of nanoparticles, nanocubes, or nanotubes. The samples described in this thesis were poured drop-wise on a glass slide until a uniform, opaque thin film of material was present.

A Bruker AXS model D8 Focus x-ray diffractometer was used for this thesis. This utilizes a copper source, producing Cu-K α radiation ($\lambda = 0.15406$ nm).

3.1.2 Microscopy

Transmission electron microscopy (TEM) is a spectroscopy technique where a sample is probed by sending electrons through the sample (see Fig. 3.2).³⁴

An electron gun releases electrons of a certain accelerating voltage towards the sample. These electrons are then focused using a series of electromagnetic lenses, which make use of the Lorentz force to fine-tune the electron beam. The electron beam travels through

the sample, which is placed between two objective lenses. This forms the image, which is projected onto a fluorescent screen. Below this, there is a charged-couple device (CCD) camera, which records the image.³⁴

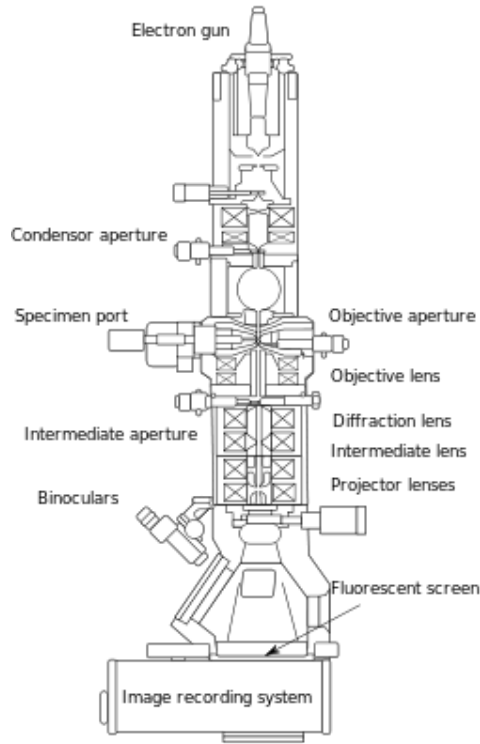


Figure 3.2: Schematic of a transmission electron microscope (taken from ref. [35]).

Contrast in the image is generated by three different types of contrast. In mass-thickness contrast, sample thickness and density determines the contrast of the image. Thicker and denser regions of the sample will appear darker than thinner and less-dense areas. The stacking of atoms in a crystalline lattice also produces a type of contrast, referred to as diffraction contrast. Areas of the sample with a perfect crystalline lattice will have higher contrast, whereas a lattice with defects will have a reduced contrast. A phase difference can exist between the direct and diffracted electrons, resulting in phase contrast. If the incident electrons have a large enough tilt, a dark-field image is produced, where a dark background

exists with the sample appearing bright. Bright-field images, which are the images used for this thesis, are the opposite, where the background is bright and the sample appears dark.³⁴

To prepare samples for TEM, they were first diluted by mixing about 1 drop of undiluted sample and 2-5 mL of solvent. One drop of this solution was then placed on a 300 mesh formvar/carbon coated grid. The grid is allowed to dry, then placed into the TEM for imaging and measurements. Size of the nanoparticles, nanocubes and nanotubes were measured using the measure arbitrary distance function on AnalySIS software.

A FEI Morgagni 268 TEM (accelerating voltage= 60kV) was used for this thesis. The operating magnification ranges from 880x to 180kx for this microscope. Images were captured using an Olympus SIS MegaView III camera.

3.2 Magnetic Measurements

Measurements of magnetization as a function of applied magnetic field were used for this thesis. This was achieved using a Vibrating Sample Magnetometer (VSM). A schematic of a VSM is shown in Figure 3.3. In this technique, the sample is placed in a uniform external magnetic field between two sensing coils, then mechanically vibrated. As a result of Faraday's Law, this motion induces a voltage in the coils that is proportional to the magnetization of the sample. The magnetization is measured in this manner at different external fields to obtain the hysteresis loop.³⁶

Starting with an external magnetic field of zero, the field is increased until the sample reaches its saturation magnetization. After this, the field is decreased back to zero, revealing the remnant magnetization. The field is then applied in the opposite direction and increased

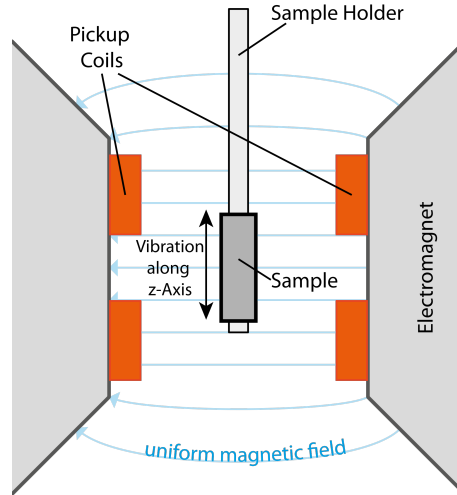


Figure 3.3: Schematic of a vibrating sample magnetometer (taken from ref. [42])

until the magnetization reaches zero, showing the coercivity of the sample. The field is increased until the sample is fully magnetized in the opposite direction. The field is decreased, then applied in the opposite direction and increased again until the saturation magnetization is achieved, completing hysteresis.¹³

Samples were prepared by either pouring them dropwise into a gel cap and allowing the solvent to evaporate or allowing the solvent to evaporate, then placing the sample into a gel cap. Any empty space in the gel cap was filled using Teflon tape, keeping the sample in place. This gel cap is then placed on the end of a probe and placed in the VSM.

For this thesis, we used a Physical Properties Measurement System (PPMS) by Quantum Design, which can achieve magnetic field strengths up to ± 7 Tesla using a helium-cooled superconducting magnet.

3.3 Hyperthermia

For this thesis, an Ambrell Easy heat system was used, which can generate an alternating magnetic field with a frequency between 150 and 400 kHz and a strength between 400 and 800 Oe.

Samples were prepared by first weighing their mass, then suspending them in water. This solution was then placed inside a coil, which produced an alternating magnetic field of a specific frequency and field strength. The change in temperature was measured using a digital temperature sensor placed in the sample. To minimize the heat contribution of the coil, the heating slope for a vial of water was subtracted from these measurements. From these measurements, the change in temperature over the change in time was calculated. The SAR was then calculated using Equation 1.1.

Chapter 4

Results

4.1 Structure, Morphology and Magnetic Properties

This section will focus on the structure and morphological properties obtained from TEM and XRD, as well as the magnetic properties obtained from VSM. The nanoparticles discussed are nickel ferrite (NiFe_2O_4).

4.1.1 Nickel Ferrite Nanoparticles

XRD

X-Ray diffraction was used to confirm the composition of our sample. According to literature, the peaks corresponding to the (220), (311), (222), (400), (422), (511) and (444) planes are characteristic of nickel ferrite nanoparticles.^{43,44} The XRD plot for this sample have clear peaks that correspond to these planes (see Fig. 4.1).

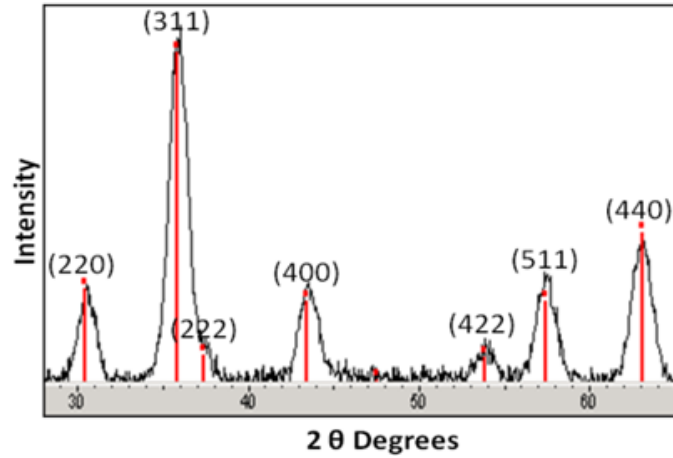


Figure 4.1: X-Ray Diffraction plot for NiFe_2O_4 nanoparticles.

TEM

Transmission Electron Microscopy was used to confirm the shape and size of the nanoparticles.

TEM images revealed that the NiFe_2O_4 particles were clearly spherical in shape with a relatively narrow size distribution (Fig. 4.2).

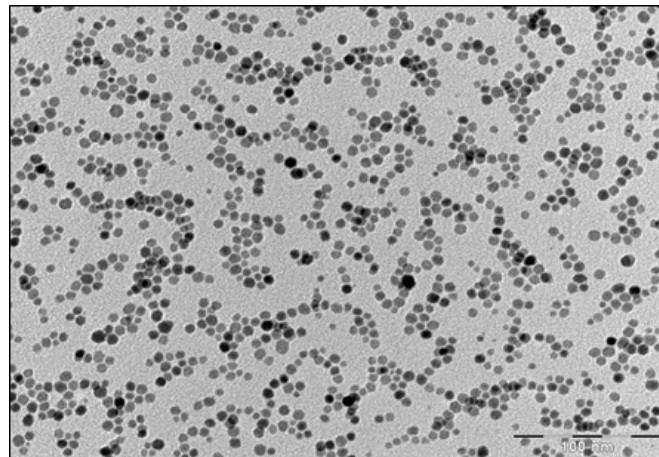


Figure 4.2: Transmission Electron Microscope image of nickel ferrite nanoparticles.

In addition, the nanoparticles are nicely dispersed, showing that the surfactants were effectively employed. The diameter of the nanoparticles were measured to be an average of 7.4 ± 1.7 nm.

4.1.2 Nanoparticle-Filled Carbon Nanotubes

TEM

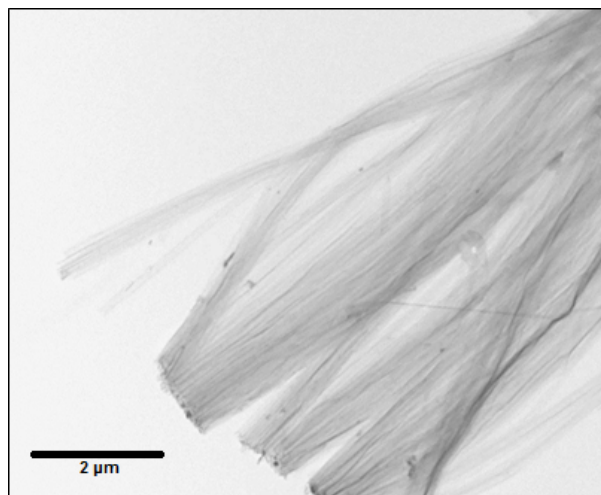


Figure 4.3: TEM image of CNTs.

Due to the catalyst-free method of synthesizing CNTs, XRD was not required to confirm the phase of the sample. TEM images were taken to determine the diameter and length of the CNTs. The outer diameter of the CNTs was determined to be 80 nm and had a length of up to 11 μm (see Fig. 4.3).

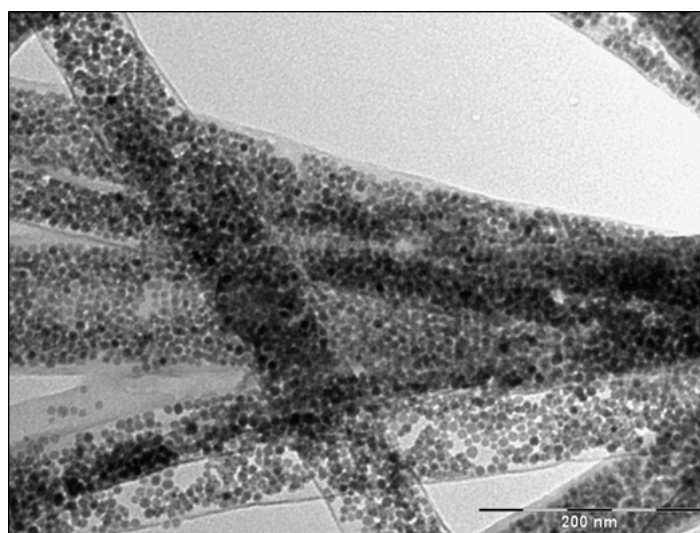


Figure 4.4: TEM image of nanoparticle-filled CNTs.

After filling the CNTs, TEM images were taken to confirm that the CNTs were successfully filled with nanoparticles. From the TEM images, we can see that there were no nanoparticles outside of the CNTs and that the CNTs were uniformly filled (see Fig. 4.4). Again, this demonstrates that the surfactants were effectively employed, preventing the nanoparticles from agglomerating.

VSM

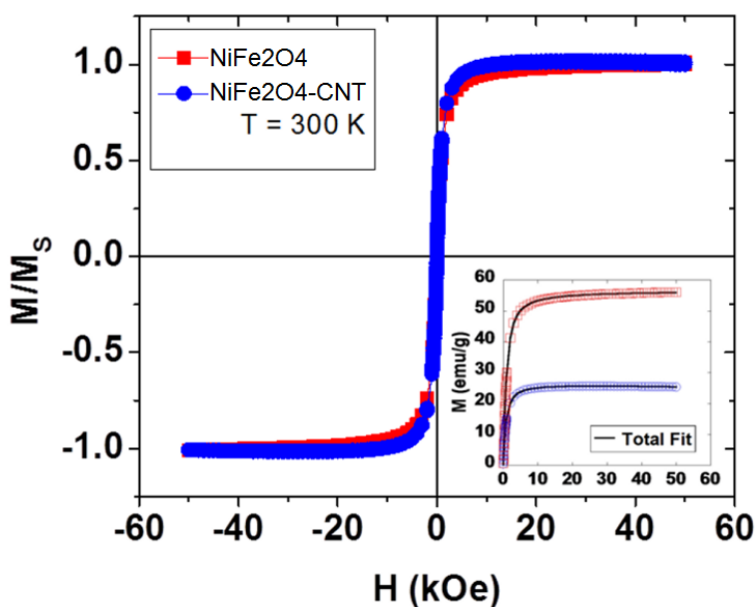


Figure 4.5: Normalized hysteresis curves for the NiFe_2O_4 nanoparticles and filled CNTs with inset comparing the saturation magnetization of the two samples.

From VSM, the M-H hysteresis curves of both the nickel ferrite nanoparticles and filled CNTs were measured. The curves were then superpositioned on the same graph to illustrate how placing the nanoparticles in the CNTs changed their magnetic properties (see Fig. 4.5). From these hysteresis curves, we were able to determine the saturation magnetization. The decrease in saturation magnetization in the case of the nanoparticle-filled CNTs (see inset of Figure 4.5) is due to the addition of the non-magnetic mass of the carbon nanotubes. Taking

the non-magnetic mass of the carbon nanotubes into account, M_S for the nanoparticle-filled CNTs should be equal to M_S for the nanoparticles alone, which was measured to be 56 emu/g. It is useful to note that the sample shows a reduced anisotropy when the nanoparticles are confined inside the CNTs. In this case, the shape anisotropy of the filled CNTs becomes significant in relation to the nickel ferrite alone.

Considering the saturation magnetization and increased significance of shape anisotropy, the nanoparticle-filled CNTs would have a higher SAR than the nickel ferrite alone.

4.1.3 Iron-Cobalt Nanocubes

XRD

The peaks characteristic of the FeCo phase are associated with the (011) and (002) planes.^{45,46}

This is in agreement with our results from XRD (see Fig. 4.6).

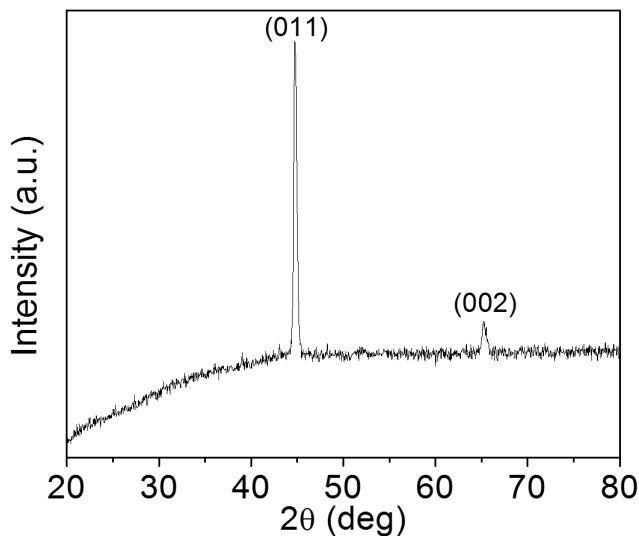


Figure 4.6: Plot showing the diffraction patterns for the FeCo sample.

TEM

From TEM we were able to see the shape and size of the nanocubes. We were first able to confirm that the nanocubes were cubic in shape (see Fig. 4.7). We were also able to see that the cubes tend to agglomerate significantly.

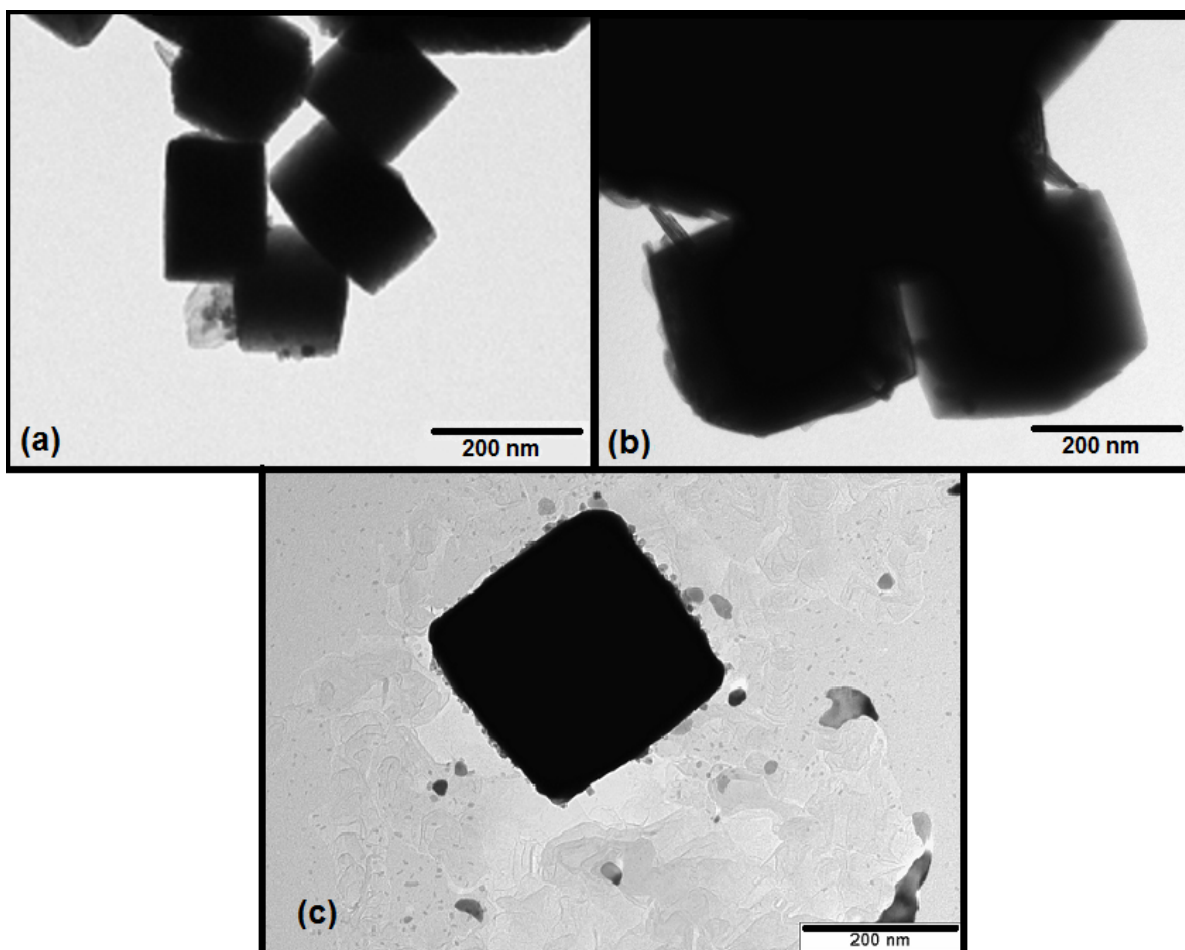


Figure 4.7: TEM images of FeCo nanocubes from the (a) 30 minute, (b) 40 minute, and (c) 50 minute reaction.

The side length was measured to be 141 ± 27 nm for the 30 minute reaction, 262 ± 53 nm for the 40 minute reaction 340 ± 42 and for the 50 minute reaction. According to Kolhatkar, et al., nanocubes with side lengths of approximately 100 nm, 200 nm, and 260 nm were synthesized using reaction times of 30, 40 and 45 minutes, respectively.²¹. Our results agree

with the positive correlation between nanocube size and reaction time, but our nanocubes are considerably larger.

VSM

From the hysteresis loop, we were able to confirm the ferromagnetic properties of the Iron-Cobalt nanocubes (see Fig. 4.8).

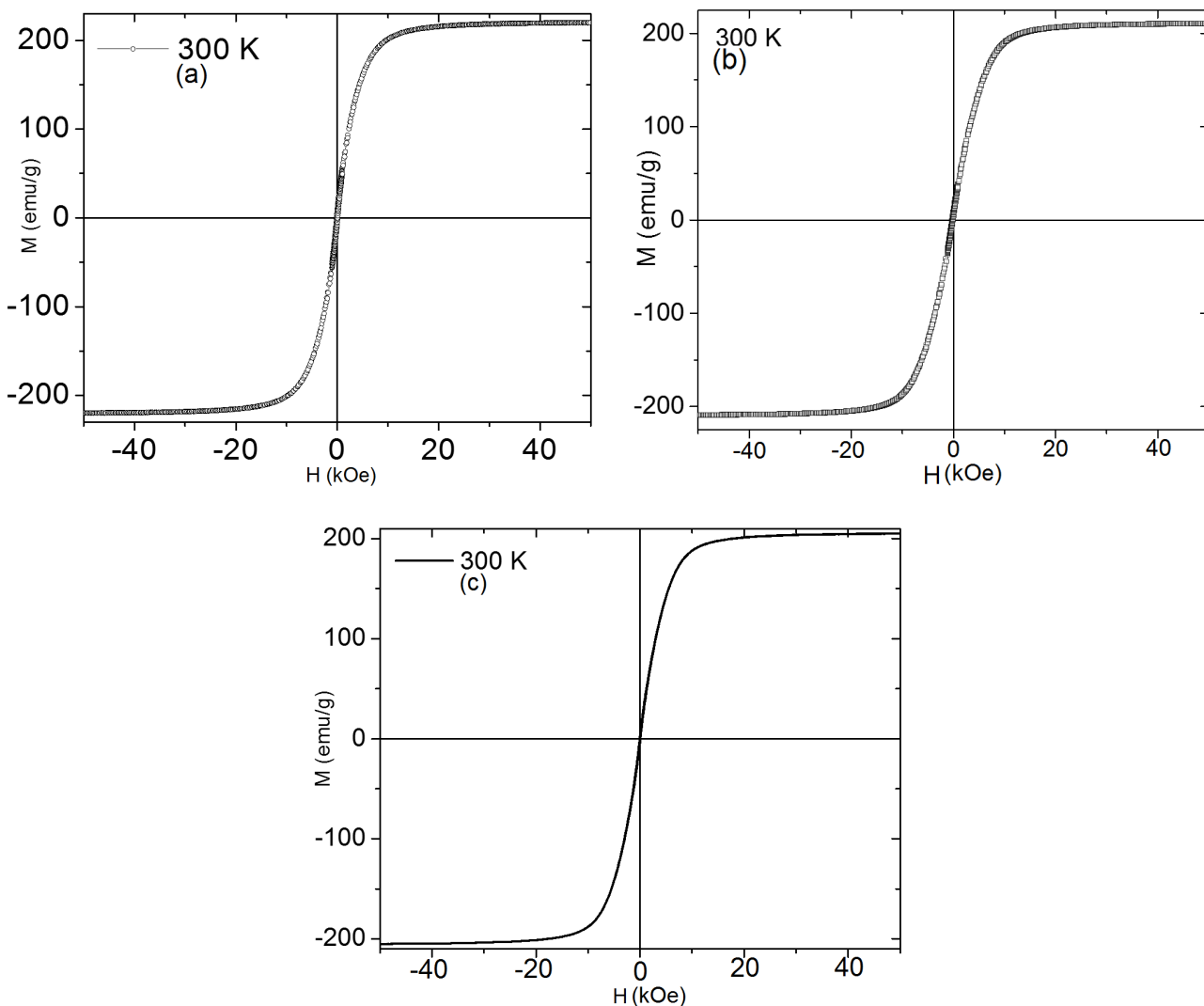


Figure 4.8: Hysteresis curves for the (a) 141 nm, (b) 262 nm, and (c) 340 nm cubes.

We found that the 141 nm cubes had a saturation magnetization of 219 emu/g, a

coercivity of 104 Oe, and a normalized magnetic remanence of 0.03; the 262 nm cubes had a saturation magnetization of 209 emu/g, a coercivity of 65 Oe, and a normalized magnetic remanence of 0.01; and the 340 nm cubes had a saturation magnetization of 204 emu/g, a coercivity of 70 Oe, and a normalized magnetic remanence of 0.01.

4.2 Hyperthermia

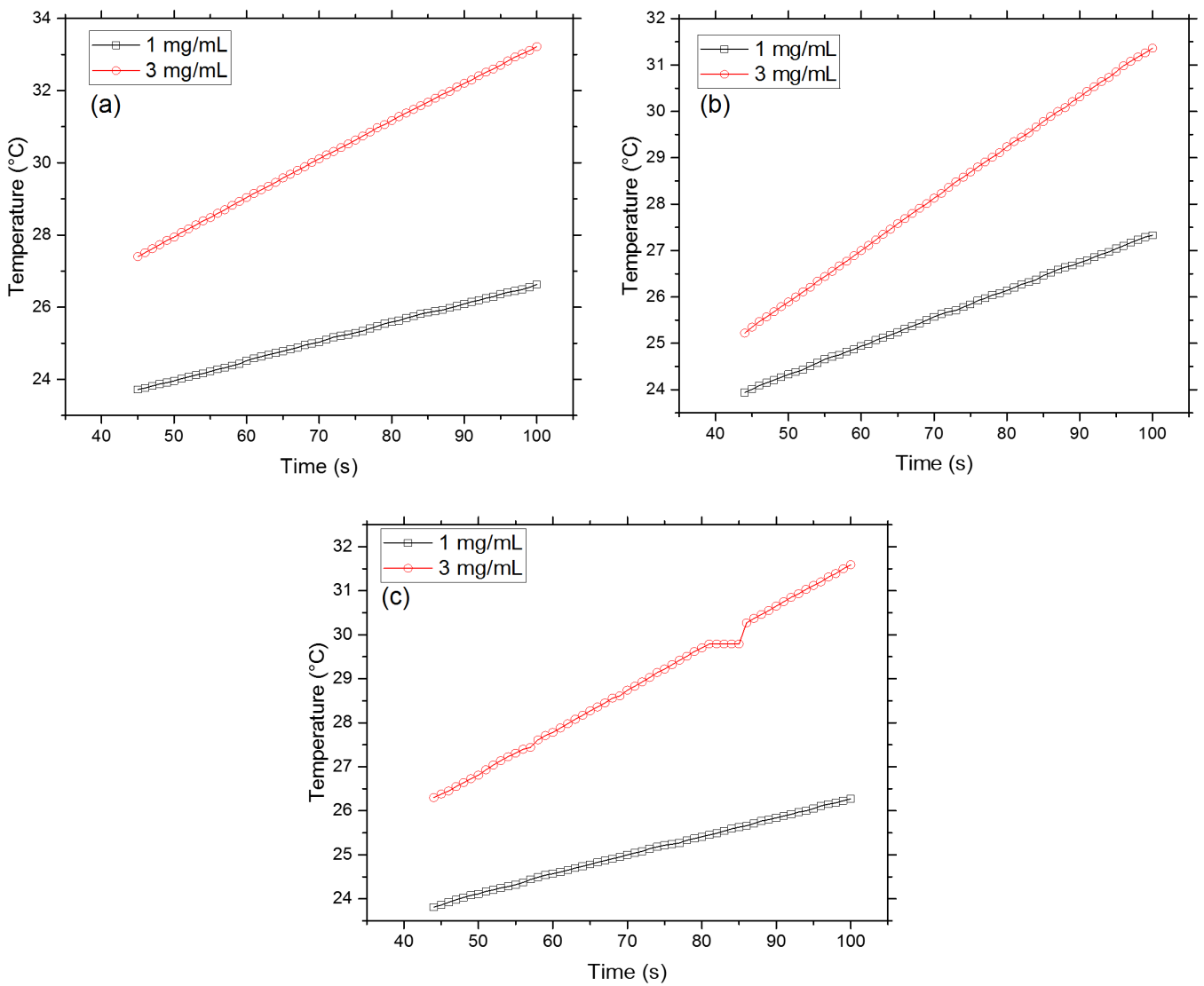


Figure 4.9: Heating curves for the (a) 141 nm, (b) 262 nm, and (c) 340 nm cubes.

Hyperthermia measurements were only taken for FeCo nanocubes. Measurements were taken for solutions with concentrations of 1 mg/mL and 3 mg/mL (see Fig. 4.9). All measurements were taken at a magnetic field frequency of 310 kHz and magnetic field strength of 800 Oe.

The change of temperature over change in time of the 142 nm nanocubes was 0.1118 C/s and 0.0531 C/s for the 3 mg/mL and 1 mg/mL solutions, respectively. This gives an SAR of 118 W/g and 109 W/g for the 3 mg/mL and 1 mg/mL solutions, respectively. The change of temperature over change in time of the 262 nm nanocubes was 0.1109 C/s and 0.0636 C/s for the 3 mg/mL and 1 mg/mL solutions, respectively. This gives an SAR of 117 W/g and 153 W/g for the 3 mg/mL and 1 mg/mL solutions, respectively. The change of temperature over change in time of the 340 nm nanocubes was 0.0945 and 0.0427 for the 3 mg/mL and 1 mg/mL solutions, respectively. This gives an SAR of 94 W/g and 66 W/g for the 3 mg/mL and 1 mg/mL solutions, respectively.

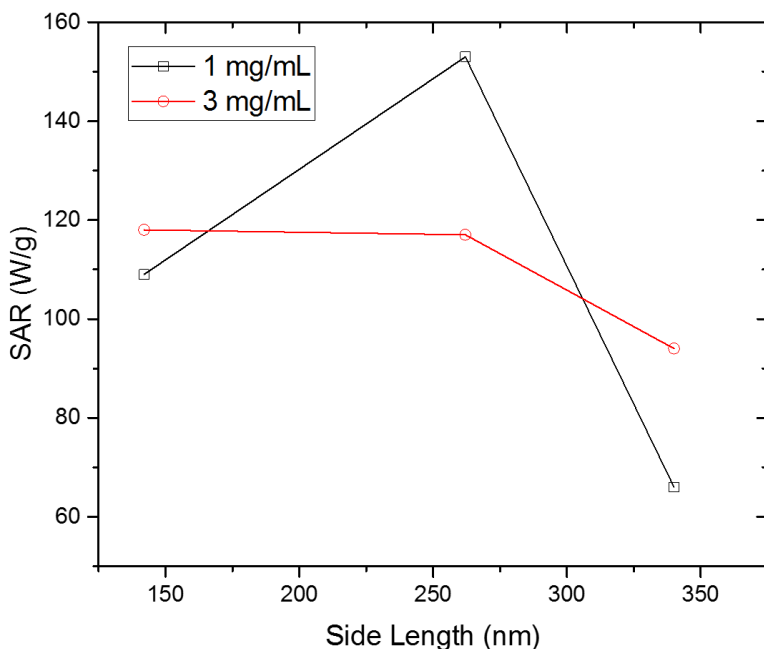


Figure 4.10: Graph studying the size-dependence of the SAR in FeCo nanocubes.

In these nanocubes, physical motion is very significant in determining the SAR. As cluster size and particle size increases, it becomes more difficult to physically rotate the nanocubes, resulting in a smaller SAR (see Fig. 4.10). This is exemplified in the 3 mg/mL case, where particles agglomerate to a greater extent than the less concentrated case. In the 1 mg/mL case, the smaller saturation magnetization and coercivity compensates for the larger size of the middle sized particles, leading to less agglomeration and a higher SAR. However, the physical rotation is greatly reduced in the biggest size, resulting in a lower SAR (see Fig. 4.10). Other factors, such as differences in surface morphologies, also contribute to the differences in SAR values.

Chapter 5

Conclusion

5.1 Conclusion of Current Work

In conclusion, we were able to successfully synthesize nickel ferrite, carbon nanotubes, and iron cobalt nanocubes and study their structure, morphology and magnetic properties. From the magnetic properties, we were able to estimate the SAR of the nickel ferrite and filled CNTs and quantify their potential as a candidate for magnetic hyperthermia. For the FeCo nanoparticles, we were able to measure the SAR.

We discussed multiple synthesis techniques for this thesis. For nanoparticle synthesis, we discussed the co-precipitation, microemulsion, hydrothermal and thermal decomposition methods, putting a special emphasis on the thermal decomposition method, which was exclusively used in this thesis for synthesis of nickel ferrite nanoparticles. For carbon nanotube synthesis, we discussed the arc-discharge, laser ablation, gas-phase catalytic growth and chemical vapor deposition (CVD) methods, putting emphasis on CVD, as it was the technique used to synthesize the CNTs of this thesis. FeCo nanocubes were synthesized

using a liquid-phase reduction reaction.

X-Ray diffraction was able to reveal the phase of the nickel ferrite nanoparticles and the FeCo nanocubes. Transmission electron microscopy was able to reveal the shape and size of the samples, while also revealing that size of FeCo nanocubes could be varied by changing only the reaction time.

From the magnetic characterizations, we were able to observe the superparamagnetic properties of nickel ferrite nanoparticles and filled CNTs, as well as the ferromagnetic properties of FeCo nanocubes. We were also able to qualitatively estimate the SAR of nickel ferrite nanoparticles and filled CNTs. From this, we found that the filled CNTs would have a larger SAR than the nanoparticles alone.

From hyperthermia measurements, we were able to measure the SAR for two different concentrations and three different sizes of FeCo nanocubes.

5.2 Future Work

Future work would focus on two things: measuring the SAR of nickel ferrite and filled CNTs, then comparing the results to the prediction described in this thesis and further investigating the heating properties of FeCo nanocubes.

Since we did not quantitatively estimate the SAR for nickel ferrite or filled CNTs, it would be useful to measure the SAR and see how they compare to other candidates for magnetic hyperthermia.

For the FeCo nanocubes, we only measured the SAR for one magnetic field strength and frequency. In order to fully investigate the heating properties of FeCo, it would be

useful to measure the heating curves for weaker field strengths and frequencies. It would also be helpful to investigate how the heating properties of FeCo are affected by different coatings, such as poly(ethylene glycol) or silica, which would influence the agglomeration of nanocubes.

Appendix A

References

1. R. Alteri, T. Bertaut, D. Brooks, et al. Cancer Facts and Figures 2015. American Cancer Society (2015).
2. N. Howlader, A.M. Noone, M. Krapcho, et al. SEER Cancer Statistics Review. National Cancer Institute (1975-2012)
3. Barack Obama: Address Before a Joint Session of the Congress on the State of the Union. (2016)
4. Treatment Types. American Cancer Society (2015).
5. A Guide to Cancer Surgery. American Cancer Society (2015).
6. What are the risks and side effects of cancer surgery?. American Cancer Society (2015).
7. Chemotherapy. National Cancer Institute (2015).
8. Chemotherapy side effects. Cancer Research UK (2015).
9. Radiation Therapy. National Cancer Institute (2015).
10. What about radiation side effects?. American Cancer Society (2015).
11. Field, S. and Bleehen, N. Hyperthermia in the treatment of cancer. Cancer Treatment Reviews 6, 63-94 (1979).
12. D. Ortega and Q. A. Pankhurst Magnetic hyperthermia. Nanoscience 1, 60-88 (2013).
13. Griffiths, D. J. Introduction to electrodynamics, 4th edition. (Prentice Hall, 2012).
14. B.M. Moskowitz, Hitchhiker's Guide to Magnetism. (1991)
15. Blundell, S., Magnetism in condensed matter. Oxford master series in condensed matter physics. 2001, Oxford ; New York: Oxford University Press. xii, 238 p.
16. Bedanta, S. and W. Kleemann, Supermagnetism. Journal of Physics D-Applied Physics, 2009. 42(1).
17. G. Vallejo-Fernandez, et al. Mechanisms of Hyperthermia in Magnetic Nanoparticles. J. Phys. D: Appl. Phys, 46, 312001 (2013).
18. A. Kolhatkar, et al. Tuning the Magnetic Properties of Nanoparticles Int. J. Mol. Sci., 14, 15977-16009 (2013)

19. B. Mehdaoui, et al. Large specific absorption rates in the magnetic hyperthermia properties of metallic iron nanocubes *J. Magn. Magn. Mater.*, 322, L49–L52 (2010)
20. Pal, S., Chandra, S., Phan, M.-H., Mukherjee, P., Srikanth, H. Carbon nanostraws: nanotubes filled with superparamagnetic nanoparticles. *Nanotechnology* 20, 485604 (2009).
21. A. Kolhatkar, et al. Cubic Silica-Coated and Amine-Functionalized FeCo Nanoparticles with High Saturation Magnetization *Chem. Mater.*, 25, 1092-1097 (2013)
22. Lu, A.H., E.L. Salabas, and F. Schuth, *Magnetic nanoparticles: Synthesis, protection, functionalization, and application. Angewandte Chemie International Edition*, 2007. 46(8): p. 1222-1244.
23. Lee, J., T. Isobe, and M. Senna, Preparation of ultrafine Fe₃O₄ particles by precipitation in the presence of PVA at high pH. *Journal of Colloid and Interface Science*, 1996. 177(2): p. 490-494.
24. Mathew, D.S. and R.S. Juang, An overview of the structure and magnetism of spinel ferrite nanoparticles and their synthesis in microemulsions. *Chemical Engineering Journal*, 2007. 129(1-3): p. 51-65.
25. Gao, G.H., et al., Shape-Controlled Synthesis and Magnetic Properties of Monodisperse Fe₃O₄ Nanocubes. *Crystal Growth and Design*, 2010. 10(7): p. 2888-2894.
26. Xie, J., et al., One-pot synthesis of monodisperse iron oxide nanoparticles for potential biomedical applications. *Pure and Applied Chemistry*, 2006. 78(5): p. 1003-1014.
27. Thostenson, E. T., Ren, Z. and Chou, T.-W. Advances in the science and technology of carbon nanotubes and their composites: a review. *Composites Science and Technology* 61, 1899–1912 (2001).
28. Iijima, S. Helical microtubules of graphitic carbon. *Nature* 354, 56–58 (1991).
29. Rinzler, A. et al. Large-scale purification of single-wall carbon nanotubes: process, product, and characterization. *Applied Physics A: Materials Science and Processing* 67, 29–37 (1998).
30. Nikolaev, P. et al. Gas-phase catalytic growth of single-walled carbon nanotubes from carbon monoxide. *Chemical Physics Letters* 313, 91–97 (1999).
31. X.W. Wei, et al. Large-Scale Controlled Synthesis of FeCo Nanocubes and Microcages by Wet Chemistry. *Chem. Mater.*, 20, 6248-6253 (2008).
32. Brandon, D.G. and W.D. Kaplan, *Microstructural characterization of materials*. 2nd ed. Quantitative software engineering series. 2008, Chichester, England: John Wiley and Sons. xiv, 536 p.
33. Ashcroft, N.W. and N.D. Mermin, *Solid state physics*. 1976, New York,: Holt. xxi, 826 p.
34. Carter, D.B.W.a.C.B., *Transmission Electron Microscopy*. 2 ed. 2009, New York: Springer.
35. *Layout of Optical Components in a Basic TEM*. Wikimedia Commons. (2009)
36. K.H.J. Buschow and F.R. de Boer. *Physics of Magnetism and Magnetic Materials*. Kluwer Academic/Plenum Publishers, 2003.
37. Vladimir Koval, Giuseppe Viola and Yongqiang Tan (2015). *Biasing Effects in Ferroic Materials, Ferroelectric Materials - Synthesis and Characterization*, Dr. Aimé Peláiz-Barranco (Ed.), InTech, DOI: 10.5772/60764.
38. *Design, Synthesis and Characterization of Biocompatible Magnetic Nanoparticles and Derived Materials for Hyperthermia*. INL, 2016.
39. Rogach, T.K.S.a.A.L., ed. *Complex-shaped Metal Nanoparticles: Bottom-Up Syntheses and Applications*. 2012, Wiley-VCH Verlag & Co. KGaA.
40. Margarita Sanchez-Dominguez, Carolina Aubery and Conxita Solans (2012). *New Trends on the Synthesis of Inorganic Nanoparticles Using Microemulsions as Confined Reaction Media, Smart Nanoparticles Technology*, Dr. Abbass Hashim (Ed.), InTech, DOI: 10.5772/33010.
41. *Magnetic Nanoparticle Synthesis*. Peter Grünberg Institute / Institute of Complex Systems. (2016)

42. Vibrating Sample Magnetometer - Sample holder and Detection Mechanism. Wikimedia Commons. (2011)
43. Baykal, A., Kasapoğlu, N., Köseoğlu, Y., Toprak, M. S. & Bayrakdar, H. CTAB-assisted hydrothermal synthesis of NiFe₂O₄ and its magnetic characterization. *Journal of Alloys and Compounds* 464, 514–518 (2008).
44. Emdadul Islam, S. K. & Sharma, P. Synthesis and Characterization of Nickel Ferrite: Role of Sintering Temperature on Structural Parameters. *Journal of Nano- and Electronic Physics*. Vol. 6 No 1, 01008(4pp) (2014).
45. Zhang, Y. et al. Synthesis and excellent electromagnetic wave absorption properties of parallel aligned FeCo@C core-shell nanoflake composites. *J. Mater. Chem. C* 3, 10813–10818 (2015).
46. Clifford, D. M., Castano, C. E., Lu, A. J. & Carpenter, E. E. Synthesis of FeCo alloy magnetically aligned linear chains by the polyol process: structural and magnetic characterization. *J. Mater. Chem. C* 3, 11029–11035 (2015).